1 **Optical properties and oxidative potential of aqueous-phase products**

2 **from OH and $^3C^*$-initiated photolysis of eugenol**

3 Xudong Li[1], Ye Tao[1], Longwei Zhu[1], Shuaishuai Ma[1], Shipeng Luo[1], Zhuzi Zhao[1],

4 Ning Sun[1], Zhaolian Ye[1,*], Xinlei Ge[2,*]

5

6 [1]College of Chemistry and Environmental Engineering, Jiangsu University of

7 Technology, Changzhou 213001, China

8 [2]Jiangsu Key Laboratory of Atmospheric Environment Monitoring and Pollution

9 Control, Collaborative Innovation Center of Atmospheric Environment and

10 Equipment Technology, School of Environmental Sciences and Engineering, Nanjing

11 University of Information Science and Technology, Nanjing 210044, China

12 *Correspondence: Zhaolian Ye (bess_ye@jsut.edu.cn) and Xinlei Ge

13 (caxinra@163.com)

14

15 **Abstract:** In ambient air, aqueous-phase oxidation may turn precursors into more

16 light-absorbing and toxic products, leading to air quality deterioration and adverse

17 health effects. In this study, we investigated eugenol degradation in the aqueous phase

18 by direct photolysis, and triplet excited organic ($^3C*$) and hydroxyl radical (OH) as

19 oxidants. Results showed degradation rates of eugenol followed the order of $^3C^*>$

20 OH>direct photolysis. Relative contributions of reactive oxygen species (ROS) and

21 $^3C^*$ were evaluated via quenching and O_2-free experiments. $^3C^*$ played a dominant

22 role in eugenol degradation for $^3C^*$-initiated oxidation, while both O_2 and

23 $O_2^{\cdot-}$generated were important for eugenol degradation for OH-initiated oxidation. Rate

24 constants under O_2, air and N_2 followed the order of $k_{O_2} > k_{Air} > k_{N_2}$ for both direct

25   photolysis and OH oxidation, and it changed to $k_{Air} > k_{N_2} > k_{O_2}$ for $^3C^*$-initiated

26   oxidation. Light absorption spectra showed absorbance at 300-400 nm, and the

27   intenstiy increased as photolysis progressed, and there were new broad fluorescent

28   spectra at excitation/emission (Ex/Em)=250/(400-500) nm, suggesting the formation

29   of new chromophores and fluorophores, such as humic-like substances (HULIS).

30   Additionally, distinct fluorescence peaks appeared at Ex/Em=(300-350)/300 nm at

31   different oxidation stages. Concentration of generated HULIS increased gradually

32   over time, then leveled off. Dithiothreitol (DTT) assay was applied to assess oxidation

33   potential of the products, which was greater than that of pure eugenol, suggesting

34   more harmful species were produced during oxidation. Detailed reaction pathways

35   were elucidated via analyses of chemical characteristics of the products.

36   **Keywords:** Aqueous phase reaction; reactive oxygen species (ROS); fluorescence

37   spectra, DTT method, oxidative potential

38

1 Introduction

40   Photochemical reactions in the atmospheric aqueous phase (cloud, fog and

41   aerosol water) affect the lifetimes of many organic species, and are important sources

42   and aging pathway of secondary organic aerosol (SOA) (Vione et al., 2006; Zhao et

43   al., 2012). Different from the gas-phase SOA, aqueous-phase SOA (aqSOA) typically

44   shows higher oxygen-to-carbon ratio (O/C), lower volatility, stronger light absorption,

45   so it plays an important role in haze formation, air quality and global climate change

46   (Ervens et al., 2011; Lim et al., 2010). However, due to the complexity of reactions

47   and influencing factors (such as precursors, oxidants, radicals and light intensity),

48   there are still many unknowns regarding the impacts of aqueous reactions. Properties

49   of the products, including optical property and oxidative potential (OP) remain

50   unclear.

51   Most laboratory studies so far have focused on aqueous phase oxidation of small

52   molecular weight VOCs, such as isoprene, terpenes (α-pinene and β-pinene), as well

53   as their gas-phase oxidation products (such as glyoxal, methylglyoxal, *cis*-pinonic

54   acid and methyl vinyl ketone) (Faust et al., 2017; Huang et al., 2011; Lee et al., 2012;

55   Zhang et al., 2010). Now concerns have been extended to semi-/intermediate volatility

56   VOCs (S/IVOCs), especially phenolic compounds, which could be produced by

57   combustion or pyrolysis of lignin in biomass (Gilardoni et al., 2016; Li et al., 2014;

58   Yu et al., 2016). Our group also has been studying aqueous phase oxidation of

59   phenolic compounds (Chen et al., 2020; Ye et al., 2020). In addition to precursors, the

60   role of radicals to aqSOA is also crucial. It is evident that liquid water contains many

61   oxidants, such as molecular oxygen (O_2), nitrate radical (NO_3), hydroxyl radical

62   (•OH), and organic triplet excited states (triplets, $^3C^*$), which play important roles in

63   photochemical oxidation reactions (Kaur and Anastasio, 2018; Scharko et al., 2014).

64   Among them, •OH is the dominant oxidant in atmospheric cloud/fog droplet/aerosol

65   water, with concentration of 10^{-13}-10^{-12} mol·L^{-1} (Arakaki et al., 2013). Hence, aqueous

66   phase •OH-induced photo-degradation has been widely studied (Sun et al., 2010; Yu

67   et al., 2016; Chen et al., 2020). Compared to OH oxidation, $^3C^*$-initiated aqueous

68   phase reaction (photosensitized reaction) has also attracted attention in the past years.

69   Several classes of organic compounds in the atmosphere, including non-phenolic

70   aromatic carbonyls, quinones, aromatic ketones and nitrogen-containing heterocyclic

71   compounds, can form $^3C^*$ after absorbing light (Kaur et al., 2019; Alegría et al., 1999;

72   Nau and Scaiano, 1996; Rossignol et al., 2014). These compounds are called

73   photosensitizers. $^3C^*$ is capable of reacting with O_2 to produce $^1O_2$ and superoxide

Atmospheric
Chemistry
and Physics
Discussions

74   radicals ($O_2^{\cdot-}$). Various reactive oxygen species (ROS) can be generated and play a

75   critical role in OH and $^3C^*$-initiated aqueous phase reactions, but so far very limited

76   studies have considered and evaluated the contribution of possible ROS species (Wu

77   et al., 2021).

78   Excitation-emission matrix (EEM) fluorescent spectroscopy, as a low-cost,

79   powerful and rapid technique, can offer detailed information on chromophores

80   therefore has been widely employed to studies of aquatic dissolved organic matter

81   (Aryal et al., 2015). However, it has not been extensively used in atmospheric aerosol

82   research (Mladenov et al., 2011). Several recent studies have investigated the

83   relationship between the optical properties and chemical structures of atmospheric

84   aerosols through combining high-resolution aerosol mass spectrometry (AMS) and

85   EEM fluorescent spectroscopy (Chen et al., 2016a; Chen et al., 2016b). Chang et

86   al.(2010) found colored products formed in the aqueous phase OH oxidation of

87   phenolic compounds. Recently, several research groups began to apply EEM

88   technique to characterize chromophores of products in the aqueous phase oxidation

89   (Chen, et al., 2016b; Chen, et al. 2019). Additionally, previous studies (Chang and

90   Thompson, 2010) showed that light-absorbing and fluorescent substances generally

91   have large conjugated moieties (i.e., quinones and polycyclic aromatic hydrocarbons

92   (PAHs)), which can damage human body. Humic-like substances (HULIS) are

93   considered as an important contributor to dithiothreitol (DTT) activity. Some

94   researchers began to pay attention to the relationship between oxidative potential (OP)

95   of water-soluble matter in $PM_{2.5}$ with chromophores (Chen et al., 2019). A variety of

96   studies take advantage of DTT assay, as a non-cellular method, to assess the OP of

97   atmospheric PM via the DTT consumption rate (Cho et al., 2005), since OP was

98   related to adverse health effect. Some other works (Fang et al., 2016; McWhinney et

99   al., 2013; Verma et al., 2015) focused on the link between chemical composition and

100   OP in PM, and has confirmed that several kinds of compounds, such as quinones,

101   HULIS and transition metals usually have large DTT activities. However, to the best

102   of our knowledge, DTT method has not been fully adapted to evaluate the OP of

103   aqueous phase oxidation products up to now.

104   In the present work, we choose eugenol as a model compound to conduct

105   aqueous phase reaction. Eugenol is a representative IVOC with moderate

106   water-solubility (2.46 g/L at 25°C). We compared the product properties under direct

107   photolysis (without oxidant) and photo-oxidation upon two radicals (•OH and ^{3}C*).

108   The characteristics of products were elucidated by combining results from

109   high-performance liquid chromatography (HPLC), ultraviolet and visible (UV-vis)

110   spectrophotometry, gas chromatography mass spectrometry (GC-MS), EEM and

111   soot-particle aerosol mass spectrometer (SP-AMS). The relative importances of

112   various ROS species for eugenol degradation was explored. This study also

113   investigated the light absorption, fluorescent and oxidative properties of the

114   aqueous-phase oxidation products.

2 Materials and methods

115

2.1 Chemicals and reagents

116

117   Eugenol (99%), tert-butanol (TBA, 99%), 3,4-dimethoxybenzaldehyde (DMB,

118   99%), para-benzoquinone (*p*-BQ, 99%), dithiothreitol (99%) and

119   5,5′-dithiobis-2-nitrobenzoic acid (DTNB, 99%) were all purchased from

120   Sigma-Aldrich chemical company. Superoxide dismutase (SOD) was from Bovine

121   Erythrocytes BioChemika. Dichloromethane (HPLC-MS grade, 99%), methanol

122   (HPLC-MS grade, 99%), acetonitrile (HPLC-MS grade, 98%), H_2O_2 (35 wt. %), and

123   2,4,6-trimethylphenol (TMP, 99%) were all obtained from Acors Chemicals. Sodium

124   azide (NaN_3, 98%) was purchased from J&K Scientific Ltd. (Beijing, China). All

125   solutions were prepared using ultrapure water (Millipore) on the day of experiments.

2.2 Photochemical experiment

127   Aqueous phase photochemical reactions were carried out in a Rayonet

128   photochemical reactor (model RPR-200), equipped with three kinds of 14W tubes (2

129   lamps of 300 nm, 7 lamps of 350 nm and 7 lamps of 419 nm) to simulate sunlight,

130   which was commonly uses as that described in George et al. (2015). Reaction solution

131   was surrounded by lamps. The lamp irradiance spectrum was recorded by using a

132   portable spectrometer (Ocean Optics Maya2000Pro) As presented in Fig.S1 in the

133   supplement, the radiation wavelength centered at 313 nm (UVB), 365 nm (UVA), 419

134   nm and 436 nm (visible region), similar to Hong et al. (2015). The light intensity at

135   the surface of the reaction solution was ~2400 $\mu W/cm^2$ in the range of 290-320 nm

136   (UVB), measured with a radiometer (Photoelectric instrument factory of Everfine

137   Corporation, Hangzhou, China).

138   The initial solution was with 300 μM eugenol. For most experiments, solution

139   was stirred and saturated by air unless otherwise stated. 300 μM H_2O_2 and 15 μM

140   DMB were added into eugenol solution as sources of •OH and $^3C^*$ radicals,

141   respectively. For $^3C^*$-mediated experiment, solutions were adjusted to pH=3 by H_2SO_4

142   in order to perform experiments under optimal conditions (Smith et al., 2014) since

143   DMB triplet state is protonated to a more reactive form in acidic solutions. We

144   conducted three sets of photolysis experiments: (A) 300 μM eugenol + 300 μM H_2O_2;

145   (B) 300 μM eugenol + 15 μM DMB; and (C) 300 μM eugenol. In each series of

146 photochemical oxidation, a dark control experiment was done synchronously with a

147 solution vessel well wrapped by aluminum foil. In addition, to evaluate the role of

148 ROS to eugenol degradation in $^3C^*$-initiated oxidation process, quenching

149 experiments using specific scavengers to quench target ROS were performed, such as

150 TBA for •OH, NaN_3 for $^1O_2$, SOD for $O_2^{•-}$, and TMP for $^3C^*$ (Wu et al., 2021). In

151 •OH-initiated oxidation process, quenching experiments using p-BQ for $O_2^{•-}$ (Raja et

152 al., 2005; Ma et al., 2019), and TBA for •OH were conducted. Further, experiment

153 were also conducted under different saturated gas (air, N_2 and O_2) in order to further

154 evaluate the role of oxygen in the photo-degradation.

2.3 Analytical methods

2.3.1 Determination of eugenol concentration

157 Before and during the irradiation, 2 mL of reacted and controlled solutions were

158 sampled periodically and subjected to HPLC (LC-10AT, Shimadzu, Japan) to quantify

159 the eugenol concentrations. HPLC was equipped with the InertSustain AQ-C18

160 reverse phase column (4.6×250 mm, 5.0 μm, Shimadzu) and a UV-vis detector. The

161 mobile phase was a mixture of acetonitrile/H_2O (v/v: 60/40) at a flow rate of 0.6

162 mL/min, and the detection wavelength was set at 280 nm. The kinetic rate constant of

163 eugenol degradation can be obtained from the slope of plot of $-\ln(c_t/c_0)$ versus

164 reaction time as presented in Eq.(1).

$$\ln(c_t/c_0)=-kt \qquad (1)$$

2.3.2 Light absorption and fluorescent spectra

167 The light absorption spectra of reacted solutions loaded in a quartz cuvette with

168   an optical length of 1 cm, were measured by using an UV-vis spectrophotometer

169   (Specord 210 plus, Analytik Jenal). The instrument is a dual-beam optical system with

170   tungsten and deuterium lamps as light sources.

171   After measurements of UV-vis, the cuvette was transferred to a

172   three-dimensional EEM fluorescence spectrometer (FluoroMax Plus， HORIBA

173   Scientific). Excitation wavelength range was 200-450 nm and emission was 290-650

174   nm, respectively. Both excitation and emission wavelength intervals were 10 nm, and

175   the integration time was 0.1 s.

2.3.3 Determination of HULIS concentration

176

177   Solid phase extraction (SPE) cartridge were used to isolate HULIS from the

178   reaction solution. The original SPE cartridges was rinsed with 1 mL ultrapure water

179   and 3 mL methanol before extraction. The solution (25 mL) was acidified to pH of 2

180   using 0.01 M HCl, then loaded on SPE cartridge, subsequently washed with 1 mL

181   ultrapure water. The HULIS part was retained on the SPE cartridge. 3 mL methanol

182   containing 2% ammonia (w/w) was added into SPE cartridge to elute HULIS

183   component, and was evaporated to full dryness with high-pure N_2, followed by

184   dilution with ultrapure water to 25 mL for quantification of HULIS with HPLC

185   coupled with an evaporative light scattering detector (ELSD3000). The recovery

186   efficiency of standard SRFA was 75-80%. The details have been described elsewhere

187   (Tao et al., 2021).

2.3.4 Oxidative potential based on DTT assay

188

189   We detected OP based on previous DTT method (Cho et al., 2005; Lin and Yu,

190   2019) with minor improvements. Briefly, a 200 μL portion of sample solution was

191   transferred into 10 mL tube, then 1 mL of 0.1 mM phosphate buffer (pH=7.4) and 50

192   µL of 2.5 mM DTT were added and mixed thoroughly. The samples were placed in a

193   dry bath at 37°C for incubation, subsequently spiked with 100 µL of 5 mM DTNB

194   (prepared in 0.1 mM phosphate buffer). Reaction between DTNB and DTT produces

195   colored 2-nitro-5-thiobenzoic (TNB), which was quantified using UV-vis

196   spectrometer within 30 min. Finally, we recorded light absorbance (A_0) at 412 nm

197   before incubation and absorbance (A_t) at different incubation time t. Another 200 µL

198   ultrapure water was treated in the same way in order to obtain blank initial light

199   absorbance value (A_0) and absorbance (A) at incubation time t. Thus, the

200   concentration of DTT consumed by the sample solution (M_{DTT}, µM) and blank

201   solution (M_{DTT0}, µM) were calculated as Eq.(2) and Eq.(3), respectively.

202
$$M_{DTT} = \frac{A_0 - A_t}{A_0} \times C_{DTT0} \tag{2}$$

203
$$M_{DTT0} = \frac{A_0 - A}{A_0} \times C_{DTT0} \tag{3}$$

204   Here, C_{DTT0} was initial DTT concentration in sample solution (100 µM in this

205   work). DTT consumption rate (R_{DTT} and R_{DTT0}) was obtained from the slope of plot of

206   M_{DTT} and M_{DTT0} versus incubation time. Experiments of blanks and samples were

207   typically run in a triplicate.

208   **2.3.5 Products analysis of products by GC-MS**

209   Reacted solution (about 30 mL) was extracted by 10 mL dichloromethane twice,

210   subsequently concentrated to 1 mL using dry N_2, transferred to a GC vial, and

211   analyzed with a GC-MS (7890A GC/5975C MS, Agilent), using a DB-5ms capillary

212   column (30 m×0.25 mm×0.5 µm). The operational conditions were set as follows:

213   injector at 200°C; ion source at 230 °C; The column oven temperature was

Atmospheric
Chemistry
and Physics
Discussions

214   programmed: held at 35°C for 4 min, then ramped to 250 °C at a rate of 20°C/min and

215   held for 10 min. The recovery efficiency, method detection limits and quality

216   assurance/quality control has been described in detail elsewhere (Ye et al., 2020).

217   **2.3.6 SP-AMS analysis and aqSOA mass yield**

218   Aerodyne SP-AMS was applied to analyze low volatile organics in reaction

219   solution, similar to our previous work (Chen et al., 2020). AMS data were acquired in

220   V mode and analyzed by Squirrel v.1.56D and Pika v1.15D software. All the organic

221   fragment ions were classified into six groups: CH, CHO_1, CHN, CHO_2, CHON, HO.

222   Elemental ratios (O/C; hydrogen-to-carbon, H/C), were obtained according to the

223   method proposed by Canagaratna et al. (2015).

224   Since the AMS analysis requires the nebulization of sample solution into

225   particles before determination, and quantification of organics in each experimental run

226   depend on atomization efficiency and carrier gas flow, we cannot use SP-AMS

227   recorded concentration to quantify aqSOA mass directly. In this case, according to the

228   method suggested by Li et al. (2014), we added an internal standard (SO_4^{2-}) prior to

229   AMS analysis. The ratio of particle-phase organics to SO_4^{2-} ($\Delta Org/SO_4^{2-}$) after

230   atomization represented the relative aqSOA mass. Furthermore, aqSOA mass yield

231   (Y_{SOA}, %), which is generated aqSOA mass per unit mass of precursor consumed, can

232   be calculated as Eq. (4).

$$Y_{SOA}(\%) = \frac{(\Delta Org/SO_4^{2-})[SO_4^{2-}]_0}{C_0 M \eta} \times 100\% \qquad (4)$$

234   Where $[SO_4^{2-}]_0$ is the initially added SO_4^{2-} concentration (here 7.27 mg·L^{-1}); C_0 is

235   initial eugenol concentration, mmol/L; M is molecular weight of precursor (164 g/mol

236   for eugenol) , η is the degradation rate of eugenol.

3 Results and discussion

3.1 Kinetics of the photo-oxidation

Figure 1 shows unreacted eugenol concentrations (c_t) and the negative logarithm of c_t/c_0 ($-\ln(c_t/c_0)$) as a function of reaction time, respectively. Error bars represent one standard deviation from replicated measurements. As described in Fig. 1, eugenol concentration decreased to be lower than 20% of the initial concentration at 3 h, suggesting photolysis was fast under all three conditions. In the presence of $^3C^*$, eugenol was degraded to nearly 100% after 3 h. Previous study in our group about $^3C^*$-initiated oxidation of 4-ethylguaiacol (Chen et al., 2020) showed that it degraded completely until 21 h. Apart from difference of target precursor, different light irradiation spectra and stronger energy of light in this work might be responsible for the fast decay of eugenol. When photon energy is higher than energy of chemical bond, they can directly decompose the compound via breaking the chemical bond. The energies of photons at 313, and 365 nm are 395 kJ/mol, and 338 kJ/mol, which are higher than certain chemical bond energies, for instance, 354 kJ/mol for C-C, and 321 kJ/mol for C-O, but lower than O-H (463 kJ/mol), C-H (410 kJ/mol). As a result, photons of 313nm and 365nm lights are able to directly break chemical bonds of eugenol molecule, leading to decomposition and possibly further mineralization. Therefore, reaction mechanisms of photo-oxidation differ with different light sources.

The first-order rate constants were obtained by fitting eugenol concentration into the equation. As shown in Fig. 1b, $\ln(c_t/c_0)$ is proportional to reaction time, and the first-order rate constants were 2.43×10^{-4} s^{-1}, 2.73×10^{-4} s^{-1}, and 5.75×10^{-4} s^{-1}, for direct photolysis, OH-initiated and $^3C^*$-initiated photo-oxidation, respectively. $^3C^*$-initiated photo-degradation was quicker than that with ·OH (5.75×10^{-4} s^{-1} vs. 2.73×10^{-4} s^{-1}),

261   which can be attributed to more ROS (such as $^1O_2$, $O_2^-\cdot$ and $\cdot OH$)   participating in

262    $^3C^*$-initiated photolysis. A similar result was found for aqueous phase photochemical

263   oxidation with three phenols by Yu et al.(2016) that degradation rates of three

264   compounds were all higher with $^3C^*$ than with OH.
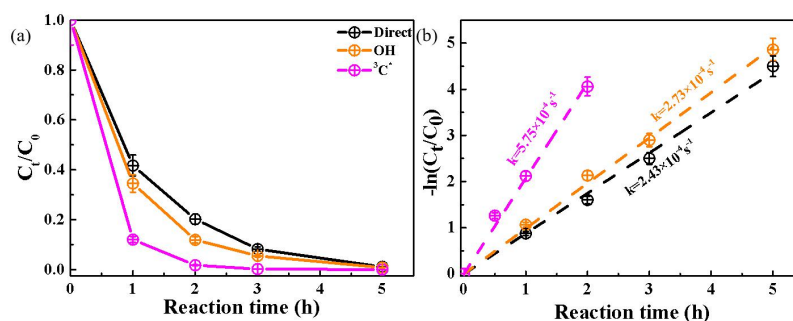
265

266   **Figure 1.** Aqueous-phase eugenol decay kinetic curves (a) and rate constants (b) under three

267   conditions. Error bars represent one standard deviation from replicated measurements.

268   **3.2 Relative importance of ROS to photo-oxidation**

269   **3.2.1 Quenching experiments in $^3C^*$-initiated photo-oxidation**

270   Relative importance of ROS in photo-degradation processes was usually

271   investigated by the addition of appropriate quenchers, and here they were calculated

272   based on the different degradation efficiencies of eugenol in absence and presence of

273   different ROS quenchers. For each scavenger, we conducted several gradient

274   experiments with varying molar ratios of eugenol to quenchers. The ratios were set as

275   0.075:1, 0.15:1, 0.3:1, 0.75:1 and 1.5:1 for quenchers of NaN_3, TMP and tert-butanol,

276   and 1.2:1, 1.6:1, 2.5:1, 5:1 and 10:1 for SOD, which were all within the typical range

277   of molar ratios to quench ROS reported previously (Zhou et al., 2018) . Fig. S2 shows

278   the effects of different ratios on eugenol degradation. As shown, when adding

Atmospheric
Chemistry
and Physics
Discussions

Open Access

EGU

279   quenchers into solution before experiments, all rate constants were lower than their

280   quencher-free companions. We finally selected the molar ratios of eugenol to

281   quencher TBA, NaN_3, TMP and SOD, of 1.5, 0.15, 0.075 and 2.5, respectively,

282   according to the maximum quenching efficiency. Fig. 2 compares the rate constants

283   determined under various quenching conditions. Compared with experiments without

284   quencher, rate constants decreased in the order of TMP > NaN_3 > SOD > TBA,

285   suggesting relative importance of ROS to degradation was in the order of $^3C^* > {}^1O_2 >$

286    $O_2^{\bullet-} > \bullet OH$. This result suggests that $^3C^*$ plays a main role in the photo-oxidation

287   reaction. Another study (De Laurentiis et al., 2013) on phenol photosensitized by the

288   triplet state of 1-nitronaphthalene (1NN) also showed $^31NN^*$ was able to degrade

289   phenol via direct reaction with phenol ($^31NN^* + phOH \rightarrow 1NN^{-\bullet} + phO^\bullet + H^+ \rightarrow products$),

290   while both OH and $^1O_2$ contributions were relatively minor.

291   The value of $(k-k_{TMP})/k$ was 0.857, therefore contribution of $^3C^*$ was estimated to

292   be as high as 85.7%. In the same way, the contributions of $^1O_2$, $O_2^{\bullet-}$ and $\cdot OH$ were

293   80.5%, 61.4% and 53.9%, respectively. The total contribution of the four ROS largely

294   exceeded 100%. This can be explained by the fact that ROS scavengers can actually

295   significantly interrupt the radical chain reactions as compared to those in the absence

296   of scavengers. For instance, the addition of TMP not only scavenge $^3C^*$, but also

297   inhibits $^1O_2$, $O_2^{\bullet-}$, etc. These findings suggest that we cannot directly obtain

298   contributions of each ROS just on basis of the scavenging efficiencies. It should be

299   cautious to apply quenching approach to quantify the role of ROS for pollutant

300   degradation in complex reaction system. Determination of ROS variability during

301   oxidation should be instead by an effective way to elucidate the role of each ROS.

302   Therefore, we tried to detect $\cdot OH$ generated during photochemical reaction using a

303   Micro electron spin resonance (ESR) spectrometer (Bruker Magnettech, Berlin,

304 Germany), but unfortunately failed since the concentrations may not meet the

305 detection limit of the instrument (Fig. S3, ESR spectra of ·OH). In contrast, we were

306 able to detect higher concentrations of $^3C^*$ using the ESR technique, which reached its

307 maximum at 30 min, then decreased slowly (Fig. S3, ESR spectra of $^1O_2$).

308 Considering the high inhibition efficiency of TMP for $^3C^*$ and high $^1O_2$ concentration,

309 we can conclude that $^3C^*$ and $^1O_2$ play relatively important roles in eugenol

310 photo-degradation.

311
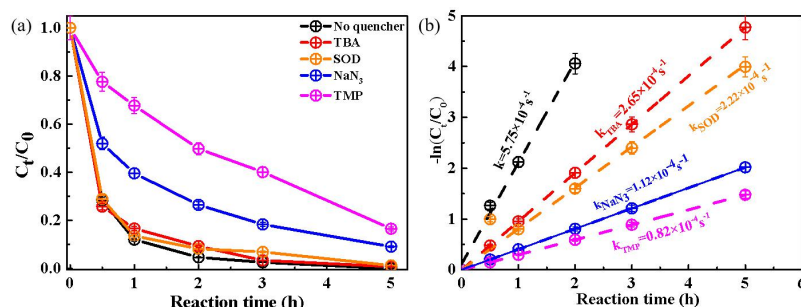
Figure 2. (a) Effect of ROS scavengers on eugenol degradation and (b) Pseudo-first-order reaction rate constants under $^3C^*$-initiated reaction. The concentration of eugenol was 0.3 mM, and the molar ratios of eugenol to quencher TBA, NaN_3, TMP and SOD, were 1.5, 0.15, 0.075 and 2.5 respectively.

3.2.2 Quenching experiments in OH-initiated photo-oxidation

317 Fig. 3a illustrates that the presences of TBA and p-BQ adversely affected eugenol

318 photolysis, suggesting that OH and $O_2^{\cdot-}$ contributed to eugenol degradation. As a

319 result, rate constant was lower than that in the absence of quenchers (Fig. 3b). The

320 molar ratios of eugenol to quenchers were set as 0.8 and 0.75 for p-BQ and TBA,

321 respectively, according to the corresponding greatest inhibitive effects from Fig. S4.

322 For TBA quenching tests, the rate constant decreased by 18.7% (from 2.73×10^{-4} s^{-1} to

323 2.22×10^{-4} s^{-1}), showing that OH radical played a minor role in eugenol photolysis.

324 Since H_2O_2 was mainly photolyzed at wavelength <300 nm to generate ·OH, but

325 irradiation wavelength of illuminant in this work was more than 300 nm. The *p*-BQ

326 could quench $O_2^{\bullet-}$, which in turn suppress the generation of other ROS (e.g., ·HO$_2$).So,

327 for the *p*-BQ quenching tests, the rate constant decreased 56% (from 2.73×10^{-4} s^{-1} to

328 1.20×10^{-4} s^{-1}), suggesting that the importance of $O_2^{\bullet-}$ was far greater than OH.

329 Therefore, we inferred that $O_2^{\bullet-}$ played a critical role in OH-initiated photolysis. This

330 hypothesis could be further confirmed by the decline of rate constant under N_2

331 saturated solution shown later.
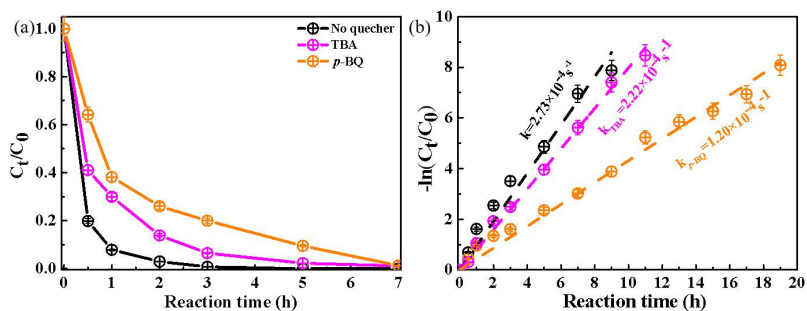
332

333 **Figure 3.** Plot of ln(C$_t$/C$_0$) versus reaction time for quenching experiments under OH system.

334 Pseudo first-order reaction rate constants (k) were also presented. The mole ratio of eugenol to

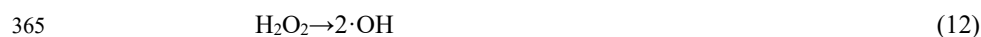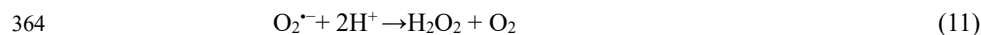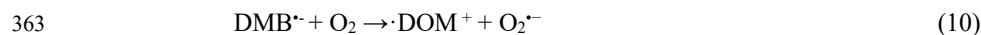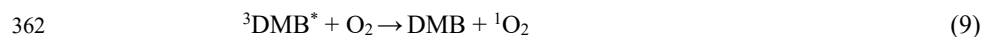335 quencher *p*-BQ and TBA was 0.8 and 0.75 respectively.
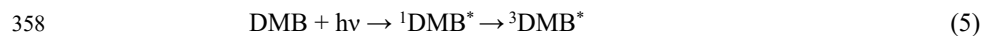
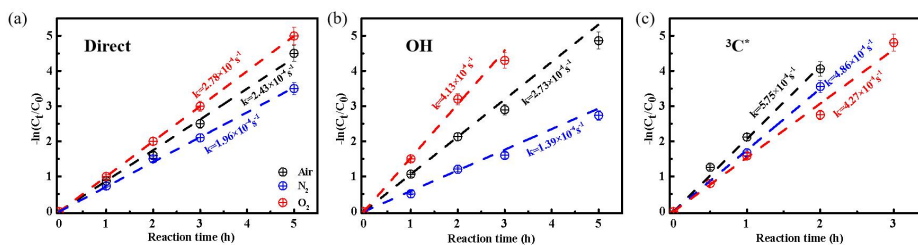336 **3.2.3 Influences of different saturated gases**

337 Oxygen-free condition was achieved by purging N_2 before experiment. Fig. S5

338 and Fig. 4 compared the eugenol decay variations and rate constants under three

339 saturated gases for direct photolysis, OH-initiated and $^3C^*$-initiated oxidation,

340 respectively. The rate constants under O_2, air and N_2 followed the order of $k_{O_2} > k_{Air} >$

341 k_{N_2} under both direct photolysis and ·OH oxidation, indicating that O_2 plays an

Atmospheric
Chemistry
and Physics
Discussions

Open Access

EGU

342　important role. Therefore in order to know the concentration variation of O_2 in the

343　solutions, the dissolved oxygen was measured. The dissolved oxygen of solution

344　decreased with reaction time shown in Fig. S6. This might be explained by the fact

345　that O_2 can act as an electron acceptor to generate $O_2^{\bullet-}$ and $HO_2\cdot$, and subsequently

346　form H_2O_2 and $\cdot OH$. For direct photolysis, rate constant under O_2 saturated condition

347　increased 14.4% while it decreased 19.3% under N_2 saturation, in contrast to the case

348　of saturated air. For $\cdot OH$ oxidation, the difference of rate constants under three

349　saturated gases became more distinct.

350　　On the contrary, rate constants followed the order of $k_{Air} > k_{N_2} > k_{O_2}$ in

351　$^3C^*$-initiated system. There are two possible explanations. On the one hand, in

352　N_2-saturated solutions, DMB would be involved in reactions (5-8), followed by more

353　effective generation of $^3DMB^*$. For this reason, eugenol degradation efficiency was

354　higher under N_2 atmosphere than in O_2-saturated solution. On the other hand, in air/O_2

355　saturated solutions, irradiation of DMB and eugenol would involve reactions (5-12),

356　as a result, $^3DMB^*$ was effectively quenched and various ROS ($^1O_2$, $O_2^{\bullet-}$, $\bullet OH$, etc)

357　were formed.

358　　　　　$DMB + h\nu \rightarrow {}^1DMB^* \rightarrow {}^3DMB^*$　　　　　　　(5)

359　　　　　${}^3DMB^* \rightarrow DMB$　　　　　　　(6)

360　　　　　${}^3DMB^* \rightarrow Products$　　　　　　　(7)

361　　　　　${}^3DMB^* + {}^1DMB^* \rightarrow DMB^{\bullet+/\bullet-}(DMB^{\bullet+}+DMB^{\bullet-})$　　　　　　　(8)

362　　　　　${}^3DMB^* + O_2 \rightarrow DMB + {}^1O_2$　　　　　　　(9)

363　　　　　$DMB^{\bullet-} + O_2 \rightarrow \cdot DOM^+ + O_2^{\bullet-}$　　　　　　　(10)

364　　　　　$O_2^{\bullet-} + 2H^+ \rightarrow H_2O_2 + O_2$　　　　　　　(11)

365　　　　　$H_2O_2 \rightarrow 2\cdot OH$　　　　　　　(12)

Figure 4. Plots of eugenol consumption versus reaction time under different saturated gases: (a) direct photolysis (b) OH-initiated and (c) $^3C^*$-initiated systems.

3.3 Optical properties of photo-oxidation products

3.3.1 Light-absorbing properties

UV-vis light spectra at different reaction times are presented in Fig. 5. We can clearly observe that the characteristic absorption peak at 280 nm of precursor decreased under all conditions due to the degradation of precursor. As seen in Fig. 5, when adding oxidant H_2O_2, the variation of light absorbance was almost the same as that without oxidant. This is consistent with the above analysis that the role of ·OH is actually weak. However, the reaction was extremely quick in the presence of $^3C^*$, and characteristic absorption peak at 280 nm after 3 h irradiation almost disappeared, suggesting nearly complete depletion of eugenol, which agrees with the results in Sect. 3.1 that more than 99% eugenol was degraded. However, note that the in $^3C^*$-systems there was still strong light absorption at wavelength <350 nm, which can be ascribed to the presence of light chromophore DMB or aqSOA products rather than precursor.

In particular, there are some differences at wavelength of 300-400 nm in the three systems. For direct photolysis and OH-initiated experiments, light absorbance at 250 nm and 300-400 nm increased during the first 15 h, then remained at a plateau until 23 h. In contrast, for $^3C^*$-initiated oxidation, light absorbance at 300-400 nm

386 increased during the first 7 h, then decreased slowly afterwards. The increase of light

387 absorbance at 250 nm demonstrates the generation of new substances upon photolysis,

388 while the enhancement at 300-400nm indicates the formation of "brown carbon"

389 species.
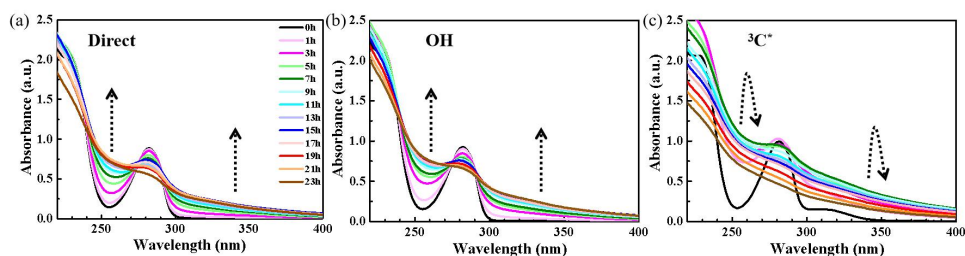
390

391 **Figure 5.** UV–Vis light absorption spectra of reacted solutions at different reaction times under

392 (a)direct photolysis, (b)OH-initiated and (c)^{3}C*-initiated systems.

3.3.2 Fluorescence properties

394   The changes of fluorescence intensities of the solutions before oxidation and

395 upon photolysis at 3 h and 7 h were investigated via the EEM technique under three

396 conditions, as shown in Fig. 6. For comparison, we also presented EEM spectra of

397 pure eugenol, pure DMB, and the end solutions (23h) of direct photolysis and

398 OH-initiated oxidation in Fig. S7. The peaks at Ex/Em=275/313 nm are due to

399 fluorescence of phenol, as suggested by Laurentiis et al. (2013). As shown in both Fig.

400 6 and Fig. S7, the fluorescence intensity at this wavelength decreased after photolysis

401 due to decomposition of eugenol, and the decreasing trend was very fast for ^{3}C*

402 oxidation. This results matched with the fast photolysis and large rate constant for ^{3}C*

403 oxidation. EEM spectra displayed similar distinct peaks at Ex/Em=250 nm/400-500

404 nm for direct photolysis and OH oxidation, which was likely attributed to

405 chromophores of HUILS (Wu et al., 2021). Previous studies have reported that

Atmospheric
Chemistry
and Physics
Discussions

Open Access

EGU

406 fluorescent compounds with emission wavelength at 400-500 nm may be highly

407 oxygenated species such as HULIS or from water-soluble secondarily formed organic

408 aerosol species (Chen et al., 2016a; Chen et al., 2019; Wu et al., 2019). For the

409 $^3C^*$-initiated reaction, extra fluorescent peaks at Ex/Em=220-300 nm/400-500nm also

410 appeared at the first 3 h, but their intensities were much weaker and gradually

411 disappeared with the propagation of photo-oxidation. Previous study (Laurentiis et al.,

412 2013) from photosensitise of phenol (nitronaphthalene as photosensitizer) also

413 showed significant increase of HULIS fluorescence signal at ex/em=330/415nm.

414   For the three systems, small fluorescence peak appeared at Ex/Em=300-350/300

415 nm at different reaction stages. Specifically, it appeared earlier for $^3C^*$ oxidation (at 3h)

416 than the other two systems, and the peak seemed to be a bit stronger in the end

417 solutions of direct photolysis and OH oxidation (Fig. S7). One unexpected

418 phenomenon in the EEM spectra here is the absence of fluorescence at higher

419 excitation wavelengths (>350 nm), which is often observed in aerosol particles (Wu et

420 al., 2021). This is likely due to the specific precursor eugenol used here as well as the

421 effect of aqueous-phase oxidation (Xie et al. 2016).

422   Note that uncertainties still exist in using EEM fluorescence technique to

423 characterize aqSOA due to lack of standard EEM profile for specific products of

424 aqueous phase oxidation and clearly more studies are needed in future.
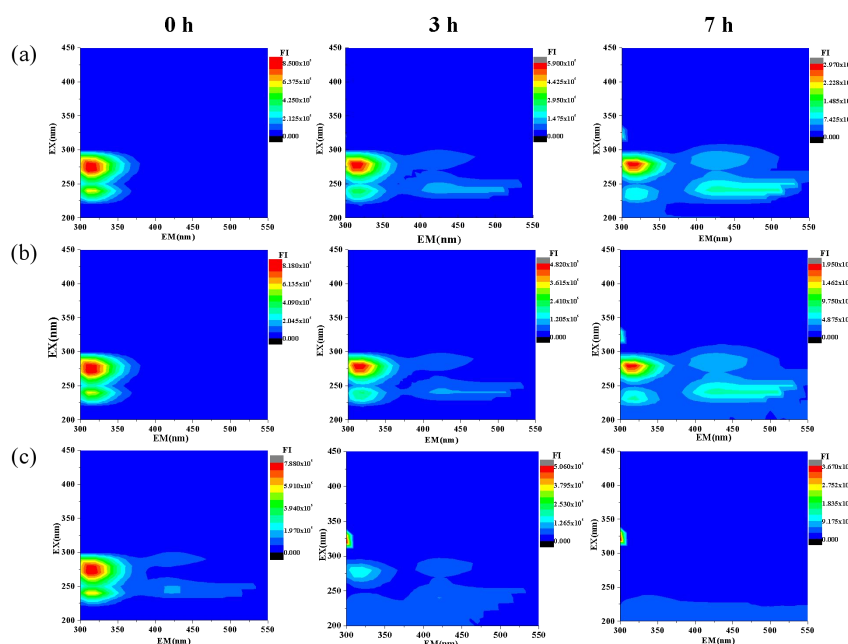
Figure 6. EEM fluorescence spectra of the initial solution (0 h) and those at different reaction time (3 h and 7 h) under (a) direct photolysis, (b) OH-initiated and (c) $^3C^*$-initiated oxidation. The right color bar represents the range of fluorescence intensity.

3.4 Generated HULIS concentration

The EEM spectra found new prominent fluorescent peak at Ex/Em=250 nm/400-500 nm, which was likely attributed to chromophores of HUILS according to results from Sect.3.3.2. However, EEM technique cannot directly distinguish products solely based on the shapes and limited information of the EEM profiles. Here we determined the HULIS concentrations in the oxidized solutions by using the HPLC method. Fig. 7 presented the measured HULIS concentrations as a function of reaction time for all three systems. The results show clearly that aqueous-phase eugenol oxidation can produce HULIS, and the amount increased gradually in the first 7 h, then remained at a similar level (about 30 mg/L) later in the OH-initiated system.

20

439   For direct photolysis, HULIS concentration increased until 11h and then retained

440   steady at a level around 40 mg/L. For the $^3C^*$ oxidation, HULIS concentration

441   increased to its maximum at 7 h, but it decreased slightly afterwards. The possible

442   reason was that generated HULIS was capable of further taking part in photochemical

443   reactions.
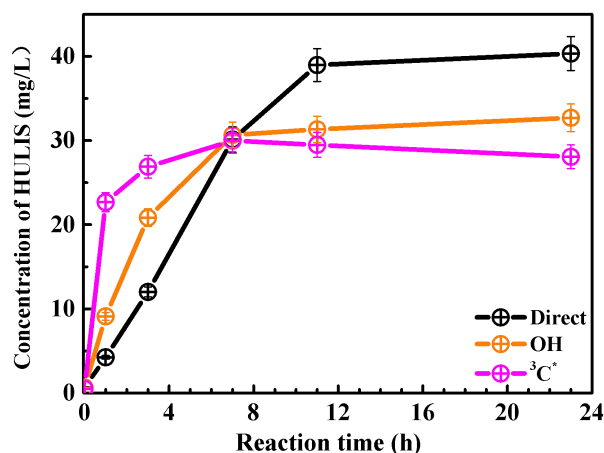
444

445   **Figure 7.** HULIS concentrations as a function of reaction time for the three systems

446   **3.5 aqSOA mass yield and oxidation degree**

447   **3.5.1 aqSOA mass yield**

448   Fig. 8a showed SP-AMS measured organic mass profiles (normalized by sulfate

449   mass, $\Delta Org/SO_4^{2-}$) against the reaction time. As the reaction propagates, $\Delta Org/SO_4^{2-}$

450   increased continuously in $^3C^*$-initiated system. Nevertheless it rose gradually and

451   reached a maximum at 19 h, then remained at a plateau for the direct photolysis and

452   OH-initiated oxidation. Fig. 8b illustrated the aqSOA mass yields at different reaction

453   times for the three systems. The aqSOA mass yields after 1h illumination were in the

Atmospheric
Chemistry
and Physics
Discussions
Open Access
EGU

454 ranges of 46.2%-196.5%, 22.1%-144.9%, 19.3%-140.1% for $^3C^*$, OH and direct

455 photolysis, respectively. And, for the same oxidation time, mass yields from

456 $^3C^*$-oxidation were generally higher than those from OH-initiated oxidation, which

457 were on the other hand, higher than those from direct photolysis.

458 The aqSOA mass yields in OH-initiated oxidation of this work agree well with

459 that reported previously for phenolic carbonyls, that is, 120% for syringaldehyde

460 (Huang et al., 2018). Our previous study on eugenol OH oxidation illuminated by a

461 500 W Xe lamp reported the aqSOA mass yield of ~180% for eugenol (Ye et al.,

462 2020), slightly higher than the value reported in this work.
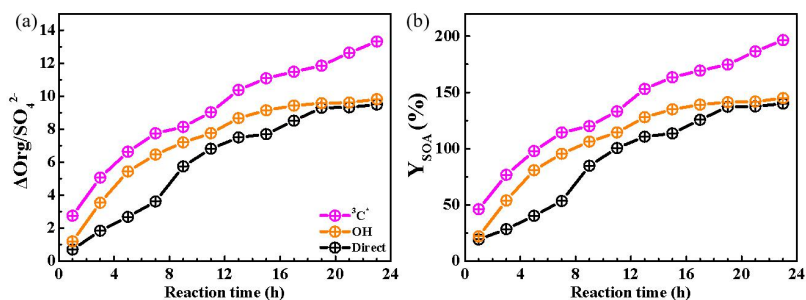
464 **Figure 8.** Variations of the aqSOA mass normalized by sulfate ($\Delta Org/SO_4^{2-}$) (a) and aqSOA mass

465 yields (b) under three photo-oxidation conditions.

466 **3.5.2 Oxidation degrees of aqSOA**

467 In order to further represent the oxidation levels of the aqSOA, O/C derived from

468 SP-AMS measured mass spectrum of the organics was used to assess oxidation degree

469 of aqSOA. In addition, carbon oxidation state (OSc, defined as 2*O/C - H/C) was also

470 calculated (Kroll et al., 2011). Fig. 9a-c described the temporal variations of the

471 elemental ratios (O/C and H/C) and OSc during oxidation in the three systems.

472 Dramatic increases of O/C and OSc in the initial stage of oxidation (within 1

473   hour) were observed, with O/C changed from 0.26 to 0.65, from 0.26 to 0.70, from

474   0.25 to 0.75, as well as OSc changed from -1.11 to -0.15, from -1.16 to -0.05, from

475   -1.13 to 0.09 for direct photolysis, OH-initiated and ^{3}C*-initiated oxidation,

476   respectively. Correspondingly, there was a clear drop of H/C in the first hour of

477   oxidation for all three systems as well. Afterwards, both O/C and OSc gradually

478   increased while H/C did not change significantly. Similarly, aqSOA from

479   ^{3}C*-oxidation had higher levels of oxidation degrees (both O/C and OSc) than that

480   from OH-oxidation, whose values were higher than that from direct photolysis. The

481   enhancements of OSc in the final solutions were 1.22, 1.11 and 0.86 for ^{3}C*-initiated

482   oxidation, OH-initiated oxidation and direct photolysis, respectively.

483   Furthermore, the f_{44} vs. f_{43} diagrams (termed as "triangle plot") can be used to

484   demonstrate the evolution of aqSOA during oxidation (Fig. 9d-f). The f_{44} and f_{43} are

485   defined as the ratios of signal intensities of m/z 44 and 43 to the total organics. The

486   results showed that the f_{44} rose continuously (moved upwards) during ·OH and ^{3}C*

487   oxidations, indicating persistent formation of organic acids, such as formic acid and

488   oxalic acid (Sun et al., 2010). Therefore pH values were measured under the three

489   systems, shown as in Fig. S8. pH values decreased from 7.38 and 7.35 to 4.7 and 4.86

490   after 1 h respectively by direct photolysis and OH-initiated oxidation. Because of the

491   adjustment of pH by H_2SO_4 in the ^{3}C* system, there was no change even though

492   organic acids were generated. Note the f_{44} enhancement was again much more

493   significant for ^{3}C* oxidation (from 0.07 to 0.16) than direct photolysis (from 0.08 to

494   0.12) and ·OH oxidation (from 0.07 to 0.13), consistent with the behaviors of O/C and

495   OSc. However, f_{43} values actually decreased in the first 3h for direct photolysis and

496   OH-initiated oxidation, and then increased at the later stages; while for the

497   3C*-initiated oxidation, it only decreased in the first hour. Note that all data points

498   located outside the f_{44} vs. f_{43} space observed for ambient aerosol AMS dataset

499   established by Ng et al. (2010), owing to the relatively lower f_{43} values.

500   In summary, our results shown here demonstrate that aqueous phase eugenol

501   photochemical oxidation can generate highly oxygenated products and hence increase

502   the degree of oxygenation of overall SOA.
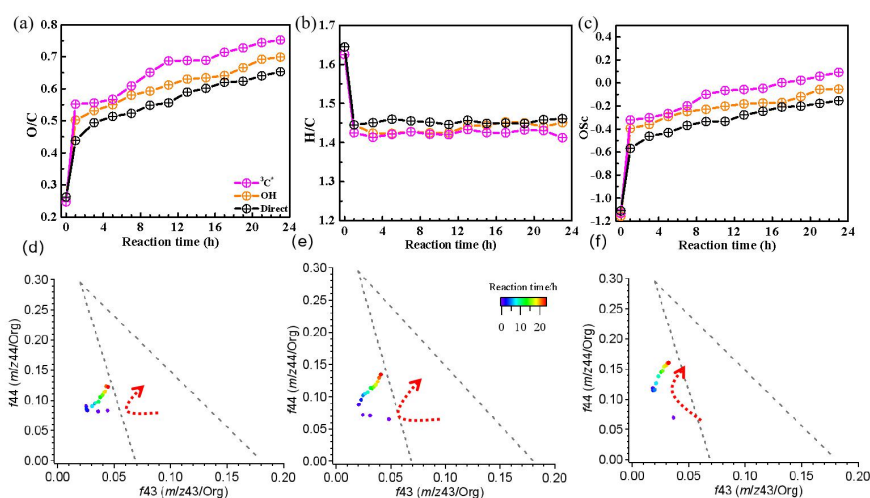
504   **Figure 9.** Variations of elemental ratios (H/C, O/C) and OSc as a function of reaction time (a-c),

505   and the "Triangle plot" of aqSOA (d-f) under direct photolysis, OH-initiated and [3]C*-initiated

506   oxidations.

3.6 Molecular characterization of products and proposed reaction mechanism

3.6.1 Molecular characterization by GC-MS

509   SP-AMS was limited to probe bulk composition of low-volatility oxidation

510   products, and the molecular characterization of products was performed by using

511   GC-MS here. For example, the total ion chromatograph (TIC) of GC-MS on the

512   solutions before oxidation (0 h) and at illumination times of 11 and 23 h for the

513   [3]C*-initiated system is shown in Fig. S9. Eugenol (retention time (RT) at 11.50 min)

514   loss was more than 90% at 11 h, which was consistent with results in Sect.3.1.

515   Comparison of products at 11h and 23h showed no significant difference. Similar to

516   results reported by our previous work (Ye et al., 2020) on the eugenol but with OH as

517   oxidant, a series of products, including 2-methoxy-4-methylphenol (molecular weight

518   (MW) 138, RT=10.27 min), vanillin (MW 152, RT=11.79 min),

519   (E)-2-methoxy-4-propenyl-phenol (MW 164, RT=12.06 min),

520   4-hydroxy-3-methoxybenzyl alcohol (MW 154, RT=12.11 min),

521   2-methoxy-4-propyl-phenol (MW 166, RT=12.18 min),

522   1-(4-hydroxy-3-methoxyphenyl)-2-propanone (MW 180, RT=12.65 min),

523   4-(1-hydroxypropyl)-2-methoxyphenol (MW 182, RT=12.73 min),

524   (E)-4-(3-hydroxyprop-1-en-1-yl)-2-methoxyphenol(MW 180, RT=12.91 min) and

525   4-allyl-methoxybenzene-1,3-diol (MW 180, RT=13.20 min) were identified in the

526   OH-initiated system. However, two additional compounds,

527   4-hydroxy-3-methoxy-mandelic acid (MW 198, RT=12.79 min) and 3,4-dihydroxy-,

528   methyl ester-benzoicacid (MW 168, RT=13.39 min) were also detected. The product

529   1-(4-hydroxy-3-methoxyphenyl) with a carbonyl group was relatively abundant.

530   Overall, there are little differences between products identified in this work and those

531   in our previous work (Ye et al., 2020), despite the different light sources and oxidants.
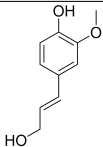
532   The molecular formulas, molecular weights, proposed structures, and identities

533   of the major products (9 compounds) are listed in Table 1 for the $^3C^*$-initiated system..

534   Except 5-ally-3-methoxybenzene-1,2-diol(MW 180, RT=12.59 min), the other eight

535   products were also detected in the OH-initiated system. Products were mainly from

536   addition/elimination of hydroxyl (-OH), methoxyl (-OCH$_3$) to benzene ring or allyl

537   group and further oxidation to carbonyl compounds, such as

538   4-hydroxy-3-methoxybenzaldehyde.

539   **Table 1.** Products identified via GC-MS detection under $^3C^*$ system

	RT (min)	Material name	Chemical structure	Chemical formula	MW (g/mol)
Product 1	10.68	4-allylphenol		$C_9H_{10}O$	134
Precursor (Eugenol)	11.50	Eugenol		$C_{10}H_{12}O_2$	164
Product 2	11.81	4-hydroxy-3-methox ybenzaldehyde		$C_8H_8O_3$	152
Product 3	12.06	(E)-2-methoxy-4-(pr op-1-en-1-yl)phenol		$C_{10}H_{12}O_2$	164
Product 4	12.11	4-(hydroxymethyl)-2 -methoxyphenol		$C_8H_{10}O_3$	154
Product 5	12.18	2-methoxy-4-propyl phenol		$C_{10}H_{14}O_2$	166
$^3C^*$ precursor (DMB)	12.29	3,4-dimethoxybenzal dehyde		$C_9H_{10}O_3$	166
Product 6	12.59	5-allyl-3-methoxybe nzene-1,2-diol		$C_{10}H_{12}O_3$	180
Product 7	12.65	4-(1-hydroxyallyl)-2 -methoxyphenol		$C_{10}H_{12}O_3$	180
Product 8	12.79	4-(1-hydroxypropyl) -2-methoxyphenol		$C_{10}H_{14}O_3$	182

| Product 9 | 12.91 | (E)-4-(3-hydroxyprop-1-en-1-yl)-2-methoxyphenol | | $C_{10}H_{12}O_3$ | 180 |

3.6.2 Reaction mechanism

Based on the GC-MS results, the reaction pathways of $^3C^*$-initiated photo-oxidation of eugenol are demonstrated in Scheme 1. To better describe pathways, DMB were expressed as [RCHO] and eugenol as Ph-R for simplicity. First, [RCHO] absorbs light and undergo excitation to $^1[RCHO]^*$, then experiences the intersystem crossing (ISC) to $^3[RCHO]^*$. The $^3[RCHO]^*$ can take part in later reactions via three channels. First, it can react with O_2 to form $^1O_2$ via energy transfer. Secondly, it can become to $[RCHO]^{\cdot-}$, subsequently react with O_2 to generate ROS $O_2^{\cdot-}$ via electron transfer, which can disproportionate to H_2O_2. The decomposition of H_2O_2 can generate OH radical. Thirdly, the $^3[RCHO]^*$ can react with Ph-R to from [Ph-R•] via H-abstraction.

As the activated intermediate [Ph-R•] was formed, it could transfer to a myriad of products by several reaction pathways. One important route is the cleavage of [Ph-R•], by dissociating into a free radical segment, such as $CH_2CH•$ or $CH_3O•$. Once the $CH_3O•$. is formed, an addition hydrogen transfer would happen, resulting in a 2H-addition to the new intermediate to form 4-allyl-phenol (product 1). Similarly, when the $CH_2CH•$ is lost, an addition of H_2O would happen on the new compound (Product 4) and further oxidized to 4-hydroxy-3-methoxybenzaldehyde (product 2). Another possibility is the intermediate [Ph-R•] could resonate to several different isoelectronic species, the radical position changing to aromatic ring or allyl group site, which would couple with HO• to form hydroxylated eugenol monomer (product 6, 7,

Atmospheric
Chemistry
and Physics
Discussions
Open Access
EGU

561   9 MW=180). Furthermore, the isoelectronic species at allyl group site could also

562   abstract a hydrogen to form isoeugenol (product 3 MW=164). Also, breakage of C=C

563   into C-C and 2H-addition at allyl group site could form 2-methoxy-4-propyl-phenol

564   (product 5, MW=166). Besides, the C=C breaking intermediate can couple with HO•

565   to form 4-(1-hydroxypropyl)-2-methoxyphenol (product 8, MW=182). In conclusion,

566    $^{3}C^{*}$ can oxidize eugenol via energy transfer, electron transfer, hydrogen abstraction,

567   proton-coupled electron transfer or other radical chain reactions. Among them,

568   electron transfer appear to be the dominant reaction mechanism.

569   The organic groups, such as methoxy, allyl groups can be eliminated from

570   aromatic ring, which then participate in photochemical reaction, resulting in

571   generation of dimers, small organic acids, CO_2 and H_2O, et al. No dimers were

572   detected in the products via GC-MS but by SP-AMS with trace amounts. The reason

573   might be because the allyl group is very active due to presence of C=C double bond,

574   providing more attacking points, favoring more functionalization and fragmentation

575   reactions.

Atmospheric
Chemistry
and Physics
Discussions

Open Access

EGU

576
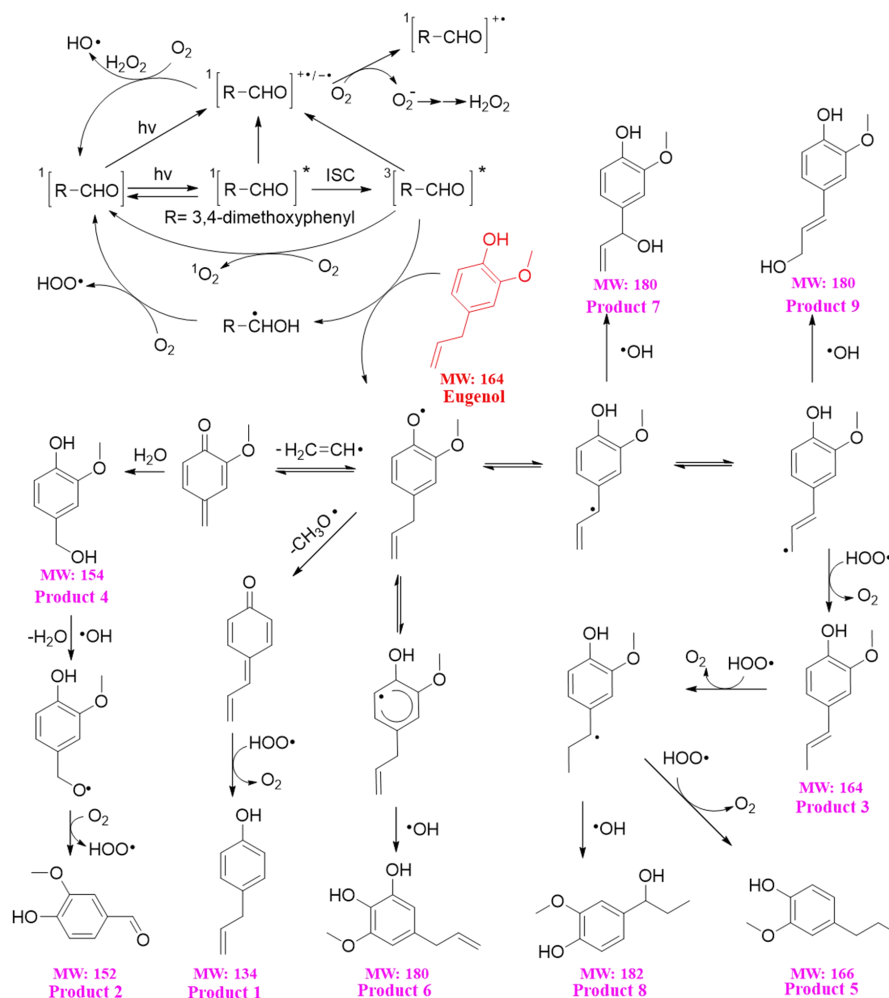
Scheme 1. Proposed eugenol $^3C^*$-initiated reaction mechanism. The red text represents the

compounds listed in Table 1 identified by the GC-MS.

3.7 Oxidative potential of products

The OP of aqueous phase products can be represented by the consumption rate of

DTT concentration per minute, defined as R_{DTT}. Fig. 10a shows the DTT consumed

mass (M_{DTT}) as a function of incubation times (0, 30, 60, 90, 120 and 150 mins) for a

triplicate sample (300 µM eugenol) and blank (ultrapure water). As shown in Fig. 10a,

29

584   M_{DTT} for both blank and eugenol were proportional to incubation time, and the slopes

585   representing DTT consumption rates were also calculated in Fig. 10a. According to

586   Fig. 10a , we obtained the average R_{DTT0} (blank) of 0.31 μM/min and R_{DTT} for initial

587   300 μM eugenol (before experiment) of 0.52 μM/min. Final DTT consumption rate

588   for reaction solution after photolysis was then blank-corrected by subtracting average

589   R_{DTT0}. Fig. 10b shows changes of blank-corrected R_{DTT} with photolysis time for direct

590   photolysis, OH-initiated oxidation and $^3C^*$-initiated oxidation, respectively. The R_{DTT}

591   value of $^3C^*$-oxidation system increased quickly and reached the maximum (0.9) at 7

592   h, then decreased slowly but its end value was slower than that from OH-oxidation.

593   The R_{DTT} value of OH-oxidation system on the other hand increased slowly and

594   reached the maximum at 21 h. The R_{DTT} value of direct photolysis system increased

595   continuously but also slowly to ~0.36 till the termination of oxidation. Nevertheless,

596   In all systems, we can see that the R_{DTT} value after oxidation was higher than that of

597   initial eugenol, providing evidence that oxidation products become overall more

598   harmful to human health than its precursor especially from $^3C^*$-initiated photolysis.

599   The DTT consumption rates are comparable to those reported by other researchers

600   using the same DTT method (Charrier and Anastasio, 2012; Lin and Yu, 2019). This

601   finding further indicates the effectiveness of DTT method to represent OPs of

602   aqueous-phase photolysis.
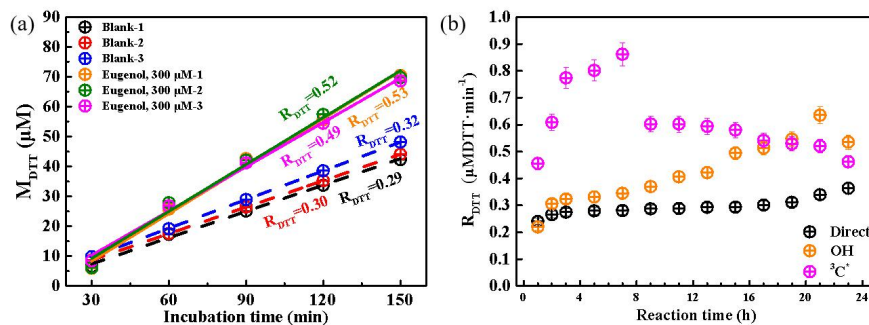
Figure 10. (a) DTT consumption mass versus incubation time for blanks and 300 μM eugenol in triplicate experiments (b) blank-corrected DTT consumption rate versus reaction time for direct photolysis, OH and $^3C^*$ induced oxidation.

4. Conclusions

This work systematically investigated the aqueous-phase photo-oxidation of eugenol. We conducted a comprehensive analysis of the degradation kinetics of eugenol, the chemical, optical as well as toxicity (oxidative potential) of the products under direct photolysis, OH-initiated oxidation and $^3C^*$-initiated oxidation in bulk aqueous-phase. Our results showed rate constants were 2.43×10^{-4} s^{-1}, 2.73×10^{-4} s^{-1}, and 5.75×10^{-4} s^{-1}, for direct photolysis, OH and $^3C^*$ photo-oxidations, respectively. Quenching experiments demonstrates the relatively importance of ROS to eugenol degradation in $^3C^*$-initiated oxidation was $^3C^* > {}^1O_2 > O_2^{\cdot-} > \cdot OH$, while both O_2 and $O_2^{\cdot-}$ played crucial role in OH-initiated reaction.

Light absorbance at wavelength of 300-400 nm in UV-vis spectra increased with photolysis time and EEM display distinct peak at ex/em=250/400-500 nm upon irradiation for direct photolysis and OH-initiated experiments. Those results all point out the generation of brown carbon and fluorophores, such as HULIS. Further HULIS

31

Atmospheric
Chemistry
and Physics
Discussions

621   determination confirmed that BrC was formed continuously over photolysis.

622   SP-AMS data showed that oxidation degree of aqSOA increased as photolysis

623   propagated, suggesting formation of highly oxidized products as well as low-volatility

624   products. A variety of products were detected via GC-MS. We then proposed that

625   functionalization was the predominant pathway throughout entire aqueous eugenol

626   oxidation. In addition, DTT consumption rate of products was in the order of

627     $^3C^*$>OH>direct, suggesting that OP of products was higher in $^3C^*$-initiated photolysis

628   process.

629   This work for the first time investigated the fluorescent properties and oxidative

630   potential of aqueous phase photo-oxidation products of eugenol, and elucidated the

631   relationship between fluorescent properties and generated HULIS. Furthermore, to

632   elucidate the role of each ROS, we should investigate the time-dependent variation of

633   all ROS via high-sensitivity EPR in future.

634   **Supplementary material**

635   The following are the Supplementary data to this article: XX

636   **Acknowledgements**

643

644

References

645

646 Alegría, A. E., Ferrer, A., Santiago, G., Sepúlveda, E., and Flores, W.: Photochemistry of water-soluble
647   quinones. Production of the hydroxyl radical, singlet oxygen and the superoxide ion, J.
648   Photochem. Photobiol. Chem., 127, 57-65, https://doi.org/10.1016/S1010-6030(99)00138-0,
649   1999.

650 Arakaki, T., Anastasio, C., Kuroki, Y., Nakajima, H., Okada, K., Kotani, Y., Handa, D., Azechi, S.,
651   Kimura, T., Tsuhako, A., and Miyagi, Y.: A general scavenging rate constant for reaction of
652   hydroxyl radical with organic carbon in atmospheric waters, Environ. Sci. Technol., 47,
653   8196-8203, https://doi.org/10.1021/es401927b, 2013.

654 Aryal, R., Lee, B. K., Beecham, S., Kandasamy, J., Aryal, N., and Parajuli, K.: Characterisation of road
655   dust organic matter as a function of particle size: A PARAFAC Approach, Water Air Soil Poll. ;
656   226, https://doi.org/10.1007/s11270-014-2289-y, 2015.

657 Canagaratna, M. R., Jimenez, J. L., Kroll, J. H., Chen, Q., Kessler, S. H., Massoli, P., Hildebrandt Ruiz,
658   L., Fortner, E., Williams, L. R., Wilson, K. R., Surratt, J. D., Donahue, N. M., Jayne, J. T., and
659   Worsnop, D. R.: Elemental ratio measurements of organic compounds using aerosol mass
660   spectrometry: characterization, improved calibration, and implications, Atmos. Chem. Phys.,
661   15, 253-272, https://doi.org/10.5194/acp-15-253-2015, 2015.

662 Chang, J. L., and Thompson, J. E.: Characterization of colored products formed during irradiation of
663   aqueous solutions containing H_2O_2 and phenolic compounds, Atmos. Environ., 44, 541-551,
664   https://doi.org/10.1016/j.atmosenv.2009.10.042, 2010.

665 Charrier, J. G., and Anastasio, C.: On dithiothreitol (DTT) as a measure of oxidative potential for
666   ambient particles: evidence for the importance of soluble transition metals, Atmos. Chem.
667   Phys. 12, 9321-9333, https://doi.org/10.5194/acp-12-9321-2012, 2012.

668 Chen, Q., Ikemori, F., and Mochida, M.: Light Absorption and excitation-emission fluorescence of
669   urban organic aerosol components and their relationship to chemical structure, Environ. Sci.
670   Technol., 50, 10859-10868, https://doi.org/10.1021/acs.est.6b02541, 2016a.

671 Chen, Q., Miyazaki, Y., Kawamura, K., Matsumoto, K., Coburn, S., Volkamer, R., Iwamoto, Y.,
672   Kagami, S., Deng, Y., Ogawa, S., Ramasamy, S., Kato, S., Ida, A., Kajii, Y., and Mochida, M.:
673   Characterization of chromophoric water-soluble organic matter in urban, forest, and marine

Atmospheric
Chemistry
and Physics
Discussions
EGU
Open Access

674   aerosols by HR-ToF-AMS analysis and excitation-emission matrix spectroscopy, Environ. Sci.

675   Technol., 50, 10351-10360, https://doi.org/10.1021/acs.est.6b01643, 2016b.

676   Chen, Q., Wang, M., Wang, Y., Zhang, L., Li, Y., and Han, Y.: Oxidative potential of water-soluble

677   matter associated with chromophoric substances in $PM_{2.5}$ over Xi'an, China, Environ. Sci.

678   Technol., 53, 8574-8584, https://doi.org/10.1021/acs.est.9b01976, 2019.

679   Chen, Y., Li, N., Li, X., Tao, Y., Luo, S., Zhao, Z., Ma, S., Huang, H., Chen, Y., Ye, Z., and Ge, X.:

680   Secondary organic aerosol formation from $^3C^*$-initiated oxidation of 4-ethylguaiacol in

681   atmospheric aqueous-phase, Sci. Total. Environ., 723, 137953,

682   https://doi.org/10.1016/j.scitotenv.2020.137953, 2020.

683   Cho, A. K., Sioutas, C., Miguel, A. H., Kumagai, Y., Schmitz, D. A., Singh, M., Eiguren-Fernandez, A.,

684   and Froines, J. R.: Redox activity of airborne particulate matter at different sites in the Los

685   Angeles Basin, Environ. Res., 99, 40-7, https://doi.org/10.1016/j.envres.2005.01.003, 2005.

686   De Laurentiis, E., Sur, B., Pazzi, M., Maurino, V., Minero, C., Mailhot, G., Brigante, M., and Vione, D.:

687   Phenol transformation and dimerisation, photosensitised by the triplet state of

688   1-nitronaphthalene: A possible pathway to humic-like substances (HULIS) in atmospheric

689   waters, Atmos. Environ., 70, 318-327, https://doi.org/10.1016/j.atmosenv.2013.01.014, 2013.

690   Ervens, B., Turpin, B. J., and Weber, R. J.: Secondary organic aerosol formation in cloud droplets and

691   aqueous particles (aqSOA): a review of laboratory, field and model studies, Atmos. Chem.

692   Phys., 11, 11069-11102, https://doi.org/10.5194/acp-11-11069-2011, 2011.

693   Fang, T., Verma, V., Bates, J. T., Abrams, J., Klein, M., Strickland, M. J., Sarnat, S. E., Chang, H. H.,

694   Mulholland, J. A., Tolbert, P. E., Russell, A. G., and Weber, R. J.: Oxidative potential of

695   ambient water-soluble $PM_{2.5}$ in the southeastern United States: contrasts in sources and health

696   associations between ascorbic acid (AA) and dithiothreitol (DTT) assays, Atmos. Chem. Phys.,

697   16, 3865-3879, https://doi.org/10.5194/acp-16-3865-2016, 2016.

698   Faust, J. A., Wong, J. P., Lee, A. K., and Abbatt, J. P.: Role of aerosol liquid water in secondary organic

699   aerosol formation from volatile organic compounds, Environ. Sci. Technol., 51, 1405-1413,

700   https://doi.org/10.1021/acs.est.6b04700, 2017.

701   George, K. M., Ruthenburg, T. C., Smith, J., Yu, L., Zhang, Q., Anastasio, C., and Dillner, A. M.: FT-IR

702   quantification of the carbonyl functional group in aqueous-phase secondary organic aerosol

703   from phenols, Atmos. Environ., 100, 230-237, https://doi.org/10.1016/j.atmosenv.2014.11.011,

704   2015.

705   Gilardoni, S., Massoli, P., Paglione, M., Giulianelli, L., Carbone, C., Rinaldi, M., Decesari, S., Sandrini,

706   S., Costabile, F., Gobbi, G. P., Pietrogrande, M. C., Visentin, M., Scotto, F., Fuzzi, S., and

707   Facchini, M. C.: Direct observation of aqueous secondary organic aerosol from

708   biomass-burning emissions, Proc. Natl. Acad. Sci. USA., 113, 10013-8,

709   https://doi.org/10.1073/pnas.1602212113, 2016.

710   Hong, J., Han, B., Yuan, N., and Gu, J.: The roles of active species in photo-decomposition of organic

711   compounds by microwave powered electrodeless discharge lamps, J. Environ. Sci. (China), 33,

712   60-8, https://doi.org/10.1016/j.jes.2014.12.016, 2015.

713   Huang, D., Zhang, X., Chen, Z. M., Zhao, Y., and Shen, X. L.: The kinetics and mechanism of an

714   aqueous phase isoprene reaction with hydroxyl radical, Atmos. Chem. Phys., 11, 7399-7415,

715   https://doi.org/10.5194/acp-11-7399-2011, 2011.

716   Huang, D., Zhang, Q., Cheung, H. H. Y., Yu, L., Zhou, S., Anastasio, C., Smith, J. D., and Chan, C. K.:

717   Formation and evolution of aqSOA from aqueous-phase reactions of phenolic carbonyls:

718   comparison between ammonium sulfate and ammonium nitrate solutions, Environ. Sci.

719   Technol., 52, 9215-9224, https://doi.org/10.1021/acs.est.8b03441, 2018.

720   Kaur, R., and Anastasio, C.: First measurements of organic triplet excited states in atmospheric waters,

721   Environ. Sci. Technol., 52, 5218-5226, https://doi.org/10.1021/acs.est.7b06699, 2018.

722   Kaur, R., Labins, J. R., Helbock, S. S., Jiang, W., Bein, K. J., Zhang, Q., and Anastasio, C.:

723   Photooxidants from brown carbon and other chromophores in illuminated particle extracts,

724   Atmos. Chem. Phys., 19, 6579-6594, https://doi.org/10.5194/acp-19-6579-2019, 2019.

725   Kroll, J. H., Donahue, N. M., Jimenez, J. L., Kessler, S. H., Canagaratna, M. R., Wilson, K. R., Altieri,

726   K. E., Mazzoleni, L. R., Wozniak, A. S., Bluhm, H., Mysak, E. R., Smith, J. D., Kolb, C. E.,

727   and Worsnop, D. R.: Carbon oxidation state as a metric for describing the chemistry of

728   atmospheric organic aerosol, Nat. Chem., 3, 133-9, https://doi.org/10.1038/nchem.948, 2011.

729   Lee, A. K. Y., Hayden, K. L., Herckes, P., Leaitch, W. R., Liggio, J., Macdonald, A. M., and Abbatt, J. P.

730   D.: Characterization of aerosol and cloud water at a mountain site during WACS 2010:

731   secondary organic aerosol formation through oxidative cloud processing, Atmos. Chem. Phys.,

732   12, 7103-7116, https://doi.org/10.5194/acp-12-7103-2012, 2012.

733   Li, Y. J., Huang, D. D., Cheung, H. Y., Lee, A. K. Y., and Chan, C. K.: Aqueous-phase photochemical

Atmospheric
Chemistry
and Physics
Discussions
Open Access
EGU

734   oxidation and direct photolysis of vanillin-a model compound of methoxy phenols from

735   biomass burning, Atmos. Chem. Phys., 14, 2871-2885,

736   https://doi.org/10.5194/acp-14-2871-2014, 2014.

737   Lim, Y. B., Tan, Y., Perri, M. J., Seitzinger, S. P., and Turpin, B. J.: Aqueous chemistry and its role in

738   secondary organic aerosol (SOA) formation, Atmos. Chem. Phys., 10, 10521-10539,

739   https://doi.org/10.5194/acpd-10-14161-2010, 2010.

740   Lin, M., and Yu, J. Z.: Dithiothreitol (DTT) concentration effect and its implications on the

741   applicability of DTT assay to evaluate the oxidative potential of atmospheric aerosol samples,

742   Environ. Pollut., 251, 938-944, https://doi.org/10.1016/j.envpol.2019.05.074, 2019.

743   McWhinney, R. D., Zhou, S., and Abbatt, J. P. D.: Naphthalene SOA: redox activity and

744   naphthoquinone gas–particle partitioning, Atmos. Chem. Phys., 13, 9731-9744,

745   https://doi.org/10.5194/acp-13-9731-2013, 2013.

746   Mladenov, N, Alados-Arboledas, L., Olmo, F .J., Lyamani, H., Delgado, A., Molina, A., and Reche, I.:

747   Applications of optical spectroscopy and stable isotope analyses to organic aerosol source

748   discrimination in an urban area, Atmos. Environ., 45, 1960-1969, https://doi.org/

749   10.1016/j.atmosenv.2011.01.029, 2011.

750   Nau, W. M., and Scaiano, J. C.: Oxygen quenching of excited aliphatic ketones and diketones, J. Phys.

751   Chem., 100, 11360-11367, https://doi.org/10.1021/jp960932i, 1996.

752   Ng, N. L., Canagaratna, M. R., Zhang, Q., Jimenez, J. L., Tian, J., Ulbrich, I. M., Kroll, J. H., Docherty,

753   K. S., Chhabra, P. S., Bahreini, R., Murphy, S. M., Seinfeld, J. H., Hildebrandt, L., Donahue,

754   N. M., DeCarlo, P. F., Lanz, V. A., Prevot, A. S. H., Dinar, E., Rudich, Y., and Worsnop, D. R.:

755   Organic aerosol components observed in Northern Hemispheric datasets from aerosol mass

756   spectrometry, Atmos. Chem. Phys., 10, 4625-4641, https://doi.org/10.5194/acp-10-4625-2010,

757   2010.

758   Raja, P., Bozzi, A., Mansilla, H., and Kiwi, J.: Evidence for superoxide-radical anion, singlet oxygen

759   and OH-radical intervention during the degradation of the lignin model compound

760   (3-methoxy-4-hydroxyphenylmethylcarbinol), J. Photochem. Photobiol. Chem., 169, 271-278,

761   https://doi.org/10.1016/j.jphotochem.2004.07.009, 2005.

762   Rossignol, S., Aregahegn, K. Z., Tinel, L., Fine, L., Nozière, B., and George, C.: Glyoxal induced

763   atmospheric photosensitized chemistry leading to organic aerosol growth, Environ. Sci.

Atmospheric
Chemistry
and Physics
Discussions

764   Technol., 48, 3218-3227, https://doi.org/10.1021/es405581g, 2014.

765 Scharko, N. K., Berke, A. E., and Raff, J. D.: Release of nitrous acid and nitrogen dioxide from nitrate

766   photolysis in acidic aqueous solutions, Environ. Sci. Technol., 48, 11991-2001,

767   https://doi.org/10.1021/es503088x, 2014.

768 Smith, J. D., Sio, V., Yu, L., Zhang, Q., and Anastasio, C.: Secondary organic aerosol production from

769   aqueous reactions of atmospheric phenols with an organic triplet excited state, Environ. Sci.

770   Technol., 48, 1049-57, https://doi.org/10.1021/es4045715, 2014.

771 Sun, Y., Zhang, Q., Anastasio, C., and Sun, J.: Insights into secondary organic aerosol formed via

772   aqueous-phase reactions of phenolic compounds based on high resolution mass spectrometry,

773   Atmos. Chem. Phys., 10, 4809–4822, https://doi.org/10.5194/acp-10-4809-2010, 2010.

774 Verma, V., Fang, T., Xu, L., Peltier, R. E., Russell, A. G., Ng, N. L., and Weber, R. J.: Organic aerosols

775   associated with the generation of reactive oxygen species (ROS) by water-soluble $PM_{2.5}$,

776   Environ. Sci. Technol., 49, 4646-56, https://doi.org/10.1021/es505577w, 2015.

777 Vione, D., Maurino, V., Minero, C., Pelizzetti, E., Harrison, M. A., Olariu, R. I., and Arsene, C.:

778   Photochemical reactions in the tropospheric aqueous phase and on particulate matter, Chem.

779   Soc. Rev., 35, 441-53, https://doi.org/10.1039/b510796m, 2006.

780 Wu, G., Ram, K., Fu, P., Wang, W., Zhang, Y., Liu, X., Stone, E. A., Pradhan, B. B., Dangol, P. M.,

781   Panday, A., Wan, X., Bai, Z., Kang, S., Zhang, Q., and Cong, Z.: Water-soluble brown carbon

782   in atmospheric aerosols from Godavari (Nepal), a regional representative of south Asia,

783   Environ. Sci. Technol., 53, 3471-3479, https://doi.org/10.1021/acs.est.9b00596, 2019.

784 Xie, M., Mladenov, N., Williams, M. W., Neff, J. C., Wasswa, J., and Hannigan, M. P.: Water soluble

785   organic aerosols in the Colorado Rocky Mountains, USA: composition, sources and optical

786   properties, Sci. Rep., 6, https://doi.org/10.1038/srep39339, 2016.

787 Ye, Z., Zhuang, Y., Chen, Y., Zhao, Z., Ma, S., Huang, H., Chen, Y., and Ge, X.: Aqueous-phase

788   oxidation of three phenolic compounds by hydroxyl radical: Insight into secondary organic

789   aerosol formation yields, mechanisms, products and optical properties, Atmos. Environ., 223,

790   117240, https://doi.org/10.1016/j.atmosenv.2019.117240, 2020.

791 Yu, L., Smith, J., Laskin, A., George, K. M., Anastasio, C., Laskin, J., Dillner, A. M., and Zhang, Q.:

792   Molecular transformations of phenolic SOA during photochemical aging in the aqueous phase:

793   competition among oligomerization, functionalization, and fragmentation, Atmos. Chem.

794   Phys., 16, 4511-4527, https://doi.org/10.5194/acp-16-4511-2016, 2016.

795   Zhang, X., Chen, Z. M., and Zhao, Y.: Laboratory simulation for the aqueous OH-oxidation of methyl

796   vinyl ketone and methacrolein: significance to the in-cloud SOA production, Atmos. Chem.

797   Phys., 10, 9551-9561, https://doi.org/10.5194/acp-10-9551-2010, 2010.

798   Zhao, R., Lee, A. K., and Abbatt, J. P.: Investigation of aqueous-phase photooxidation of glyoxal and

799   methylglyoxal by aerosol chemical ionization mass spectrometry: observation of

800   hydroxyhydroperoxide formation, J. Phys. Chem. A., 116, 6253-63,

801   https://doi.org/10.1021/jp211528d, 2012.

802   Zhou, Z., Chen, B., Qu, X., Fu, H., and Zhu, D.: Dissolved black carbon as an efficient sensitizer in the

803   photochemical transformation of 17#-estradiol in aqueous solution, Environ. Sci. Technol., 52,

804   10391-10399, https://doi.org/10.1021/acs.est.8b01928, 2018.